Inversion algorithms for the spherical Radon and cosine transform

A K Louis[1], **M Riplinger**[1], **M Spiess**[2] **and E Spodarev**[2]

[1] Institute of Applied Mathematics, Saarland University, 66041 Saarbrücken, Germany
[2] Institute of Stochastics, Ulm University, 89069 Ulm, Germany

E-mail: louis@num.uni-sb.de, riplinger@num.uni-sb.de, malte.spiess@uni-ulm.de, evgeny.spodarev@uni-ulm.de

Abstract. We consider two integral transforms which are frequently used in integral geometry and related fields, namely the cosine and the spherical Radon transform. Fast algorithms are developed which invert the respective transforms in a numerically stable way. So far, only theoretical inversion formulas or algorithms for atomic measures have been derived, which are not so important for applications. We focus on the two and three-dimensional case, where we also show that our method leads to a regularization. Numerical results are presented and show the validity of the resulting algorithms. First, we use synthetic data for the inversion of the Radon transform. Then we apply the algorithm for the inversion of the cosine transform to reconstruct the directional distribution of line processes from finitely many intersections of their lines with test lines (2D) or planes (3D), respectively. Finally we apply our method to analyze a series of microscopic two- and three-dimensional images of a fibre system.

AMS classification scheme numbers: 45Q05,65N21,60D05,44A05,44A12

1. Introduction

In this paper, we consider two integral transforms in $\mathbb{R}^d$, namely, the spherical Radon transform and the cosine transform which are closely related. For even functions f on the $(d-1)$-dimensional sphere the *spherical Radon transform* is defined as

$$Rf(\eta) = \frac{1}{\omega_{d-2}} \int\limits_{\mathscr{S}^{d-1}\cap\eta^\perp} f(\omega)\,\mathrm{d}\omega, \quad \eta \in \mathscr{S}^{d-1},$$

where $\mathrm{d}\omega$ is the spherical surface area measure. Here, the constant $\omega_{d-2} := \omega_{d-2}(\mathscr{S}^{d-2})$, which is the surface area of the $(d-2)$-dimensional unit sphere, guarantees that the transform maps constant functions to themselves. Not to be confused with the integral operator $SMf(x,r) = \int\limits_{z\in S(x,r)} f(z)\mathrm{d}a(z)$, where $S(x,r) = \{y : |x-y| = r\}$ and $\mathrm{d}a$ is the normalized area measure, which is also called spherical Radon transform. The *cosine transform* is given by

$$Cf(\eta) = \int\limits_{\mathscr{S}^{d-1}} |\langle\eta,\omega\rangle|\, f(\omega)\,\mathrm{d}\omega, \quad \eta \in \mathscr{S}^{d-1}.$$

Our aim in this paper is to invert both transforms in a numerically stable way. Therefore we use the method of the approximate inverse to develop fast numerical reconstruction algorithms. Our method can be applied for arbitrary dimensions, but we restrict our calculations to the most interesting cases $d = 2,3$ for the cosine transform, and $d = 3$ for the Radon transform, respectively.

One should remark that the method presented in this paper can also be applied to the following family of transforms, although this is not explicitly discussed in the rest of the paper:

$$Tf(\eta) = \int_{\mathcal{S}^{d-1}} h(\langle \eta, \omega \rangle) f(\omega) \, \mathrm{d}\omega, \qquad \eta \in \mathcal{S}^{d-1},$$

where $f \in L^2_e(\mathcal{S}^{d-1})$, and $h \in L^2[0,1]$. For example, the choice of $h(x) = \sqrt{1-x^2}$ leads to the well-known sine transformation.

The cosine transform plays an important role in many applications. For example, the directional distribution of a stationary line or fibre process can be estimated from intersections of its lines (or fibres) with test planes. For a fibre process Ξ, the intensity of $\Xi \cap \eta^{\perp}$ is called the *rose of intersections*, denoted by $g(\eta)$, and it is well-known that it is the cosine transform of the directional distribution of Ξ up to a multiplicative constant. In case of Ξ having a directional distribution with density φ w.r.t. the spherical surface area measure this can be written as

$$g(\eta) = \frac{\lambda}{\omega_{d-1}} C\varphi(\eta), \tag{1}$$

where λ denotes the intensity of Ξ. Thus, an even measure on the unit sphere has to be estimated from finitely many values of its cosine transform. For this purpose, stable numerical inversion algorithms are needed. In the final section we apply our method to microscopic images of the gas diffusion layer of a fuel cell, see Figure 1, to estimate the rose of directions for the fibres.

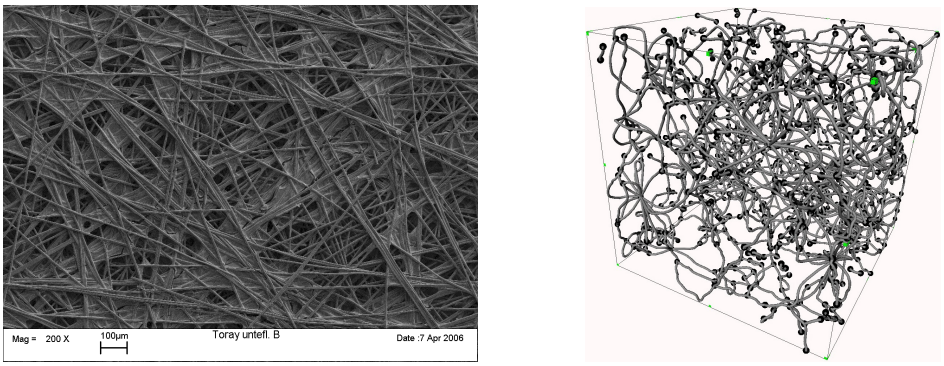

(a) 2D image of a GDL

(b) Skeleton of a 3D image of a GDL, generated with Avizo

Figure 1. Images of a gas diffusion layer (courtesy of the Centre for Solar Energy and Hydrogen Research, Ulm)

In 2005 Kiderlen and Pfrang ([1]) presented three non-parametric algorithms to estimate the rose of directions of a spatial fibre system. They are based on least square or other

optimization problems. To be able to determine the rose of directions numerically, they restrict their considerations to atomic measures. Hoffmann [2] used in 2007 also a least square estimator to invert the sine transform. There exist convergence results and a proof of consistency ([3]) for these algorithms. But on the other hand all these algorithms only lead to discrete reconstructions, which are concentrated only on a finite number of points and look often artificial. Continuous reconstructions, which provide the chance of better model fits, are missing so far in the literature.

The spherical Radon transform is frequently considered in tomography, for instance for the reconstruction of convex bodies from the area of their projections onto 2-dimensional subspaces, or in connection with intersection bodies, see also [4].

The paper is organized as follows. In the next section, we present some properties of the integral transforms under consideration. After this, we introduce the concept of the approximate inverse in Section 3.1. Since in many applications the solutions of inverse problems have to be non-negative (as e.g. in the case of probability density functions), we turn to the question of positiveness of our solution in Section 3.2. In Section 4 we calculate reconstruction kernels for the cosine transform ($d = 2$), and in Section 5 for both the spherical Radon and the cosine transform ($d = 3$). In Section 6 we characterize mollifiers, which lead to regularizations. Finally, we provide some numerical tests in the last two sections. First we illustrate our results for the spherical Radon and cosine transform with simulated data (Section 7), then we use image data of a gas diffusion layer of a PEM fuel cell to estimate the directional distribution of its fibres (Section 8).

2. Some properties of the transforms and analytic inversion results in $\mathbb{R}^d$

In this section, we present some basic facts about the two transforms, which are of importance for our algorithms. An overview of these and other properties can be found in [4, Appendix C] and [5, Chapter 3]. Denote by $C_{\mathrm{e}}^k(\mathscr{S}^{d-1})$ the space of all even k times differentiable functions f and by $L_{\mathrm{e}}^2(\mathscr{S}^{d-1})$ the space of all even square integrable functions. For $d \geq 3$ both transforms are closely related. Defining the block operator by

$$\square = \frac{\Delta_0 + d - 1}{2\omega_{d-1}}, \tag{2}$$

it can be shown that (see [6])

$$\square C = R. \tag{3}$$

Here Δ_0 denotes the Beltrami-Laplace operator on $\mathscr{S}^{d-1}$. The following properties hold in the case $d \geq 3$ for the Radon transform and in the case $d \geq 2$ for the cosine transform. It is known that for even bounded integrable functions both transforms are injective. In addition, both transforms are bijections of $C_e^\infty(\mathscr{S}^{d-1})$ to itself. More precisely, for $g_1 \in C_e^{2\lfloor (d+1)/2 \rfloor}(\mathscr{S}^{d-1})$, $g_2 \in C_e^{2\lfloor (d+3)/2 \rfloor}(\mathscr{S}^{d-1})$ there exist continuous even functions f_1 and f_2 such that $Rf_1 = g_1$ and $Cf_2 = g_2$ (see [5, Proposition 3.6.4]). Here $\lfloor x \rfloor$ denotes the integer part of $x \in \mathbb{R}$. Furthermore,

the transforms are self-adjoint in the following sense:

$$\langle f, Rg\rangle_{L^2(\mathscr{S}^{d-1})} = \int\limits_{\mathscr{S}^{d-1}} f(\omega) Rg(\omega) d\omega = \int\limits_{\mathscr{S}^{d-1}} Rf(\omega) g(\omega) d\omega = \langle Rf, g\rangle_{L^2(\mathscr{S}^{d-1})}, \quad d \geq 3 \quad (4)$$

$$\langle f, Cg\rangle_{L^2(\mathscr{S}^{d-1})} = \int\limits_{\mathscr{S}^{d-1}} f(\omega) Cg(\omega) d\omega = \int\limits_{\mathscr{S}^{d-1}} Cf(\omega) g(\omega) d\omega = \langle Cf, g\rangle_{L^2(\mathscr{S}^{d-1})}, \quad d \geq 2.$$

For the cosine transform, this follows directly from Fubini's theorem, for the Radon transform see [5]. To qualify the ill-posedness of the transforms we need to introduce Sobolev spaces on the unit sphere. A function $f \in L^2(\mathscr{S}^{d-1})$ can be expanded with respect to the spherical harmonics Y_{lm}

$$f = \sum_{l=0}^{\infty} \sum_{m=1}^{N(d-1,l)} \hat{f}_{lm} Y_{lm}$$

where $N(d-1,l) = \binom{l+d-2}{l} - \binom{l+d-4}{l-2}$ and the Fourier coefficients are given by

$$\hat{f}_{lm} = \langle f, Y_{lm}\rangle.$$

A function f lies in the Sobolev space H^s of order s if and only if $\sum_{l=0}^{\infty} \left(l^2+1\right)^{s/2} \sum_{m=1}^{N(d-1,l)} \hat{f}_{lm} Y_{lm}$ lies in L_2, and for such functions we introduce the norm

$$\|f\|_{H^s}^2 = \sum_{l=0}^{\infty} \left(l^2+1\right)^s \sum_{m=1}^{N(d-1,l)} |\hat{f}_{lm}|^2.$$

Strichartz ([7]) showed that for even functions $f \in H^s(\mathscr{S}^{d-1})$, there exist constants $b, c > 0$ such that

$$\begin{aligned} b^{-1}\|f\|_{H^s} \;&\leq\; \|Rf\|_{H^{s+(d-2)/2}} \;\leq\; b\|f\|_{H^s} \\ c^{-1}\|f\|_{H^s} \;&\leq\; \|Cf\|_{H^{s+(d+2)/2}} \;\leq\; c\|f\|_{H^s} \end{aligned} \quad (5)$$

(see also [6]). For both transforms there exist analytic inversion formulas even in more general settings. Helgason obtained in [8] an analytic inversion formula for the spherical Radon transform, which was modified in [9] to a more compact form:

Theorem 1. For $f \in C_e(\mathscr{S}^d)$ and $d \geq 3$ holds:

$$f(\xi) = \frac{(-1)^{d-2} 2^{d-3}}{(d-3)!\,\omega_{d-1}} \left(\frac{\partial}{\partial(\mu^2)}\right)^{d-2} \left[\int\limits_{\langle \xi,\omega\rangle^2 > \mu^2} \frac{Rf(\omega)|\langle \xi,\omega\rangle|}{(\langle \xi,\omega\rangle^2 - \mu^2)^{\frac{4-d}{2}}} \mathrm{d}\omega\right]_{\mu=0}, \qquad \xi \in \mathscr{S}^{d-1}.$$

While this formula forms a proper basis for theoretical considerations, it can not be used for numerical calculations, because of their numerical instability.

Other analytic inversion formulas, also for the case $f \in L_e^p(\mathscr{S}^{d-1})$, are presented in [10]. In this paper, a backprojection algorithm for the inversion of the Radon transform is proposed and some conditions for a function a are given, such that for $f \in L_e^p(\mathscr{S}^{d-1})$

$$\lim_{\varepsilon \to 0} \frac{1}{\varepsilon^{d-1}} \int\limits_{\mathscr{S}^{d-1}} a\left(\frac{\sin[d_{\mathrm{geo}}(\xi,\omega)]}{\varepsilon}\right)(Rf)(\omega)\,\mathrm{d}\omega = \alpha f(\xi), \qquad \xi \in \mathscr{S}^{d-1},$$

holds in the L^p-Norm, where d_{geo} denotes the geodesic distance and α is a constant depending on a. This complies with the theoretical idea behind our algorithms as well.

Unfortunately, it is difficult to find a function a which fulfils the conditions. In [10] there is an example which leads to

$$a(\tau) = \tau \frac{-\tau^2/2 + \mathrm{i}}{(\tau^2 + \mathrm{i})^{\frac{5}{2}}},$$

but the resulting inversion formula does not work numerically, since the function oscillates very strongly and so a stable numerical calculation is not possible. This is not surprising, because no regularization is applied.

3. Approximate inverse

3.1. The method

The method of the approximate inverse, introduced in [11], is a powerful and versatile tool for deriving fast regularization methods for stabilizing the inversion in various applications, see for example [12], [13] or [14]. Likht [15] reported already in 1967 that the calculation of linear functionals of the solution of inverse problems stabilizes the inversion method. Here, we want to solve $Tf = g$, where T is the spherical Radon transform or the cosine transform with $f, g \in L^2_e(\mathscr{S}^{d-1})$. The idea behind our algorithms is to calculate a "smoothed version" of the solution, namely

$$f_\gamma(\eta) := \int_{\mathscr{S}^{d-1}} f(\omega) e_\gamma(\eta, \omega) \mathrm{d}\omega, \qquad \eta \in \mathscr{S}^{d-1}, \tag{6}$$

with

$$f_\gamma \to f \quad \text{in some sense (cf. Remark 2) as} \quad \gamma \searrow 0.$$

We also demand that the *mollifier* $e_\gamma : \mathscr{S}^{d-1} \times \mathscr{S}^{d-1} \to \mathbb{R}_+$ is even in both arguments and has the property

$$\int_{\mathscr{S}^{d-1}} e_\gamma(\eta, \omega) \mathrm{d}\omega = 1 \qquad \text{for any } \eta \in \mathscr{S}^{d-1}. \tag{7}$$

We restrict our attention to non-negative mollifiers, cf. Subsection 3.2. Nevertheless most calculations can be also done for mollifiers with negative values. Then, for a given mollifier, the reconstruction kernel ψ_γ is determined by the solution of

$$T\psi_\gamma(\eta, \cdot) = e_\gamma(\eta, \cdot). \tag{8}$$

Note that e_γ belongs to the range of T, if it lies in $C^k_e(\mathscr{S}^{d-1})$ for k sufficiently large (cf. Section 2). Using (4), we arrive at

$$\begin{aligned} f_\gamma(\eta) &= \langle f, e_\gamma(\eta, \cdot) \rangle_{L^2(\mathscr{S}^{d-1})} = \langle f, T\psi_\gamma(\eta, \cdot) \rangle_{L^2(\mathscr{S}^{d-1})} \\ &= \langle Tf, \psi_\gamma(\eta, \cdot) \rangle_{L^2(\mathscr{S}^{d-1})} = \langle g, \psi_\gamma(\eta, \cdot) \rangle_{L^2(\mathscr{S}^{d-1})} =: T_\gamma g(\eta). \end{aligned} \tag{9}$$

Remark 1. The calculation (8) is independent of the given right hand side in $Tf = g$. Therefore it can be carried out before the reconstruction of f starts. This leads to efficient algorithms for the calculation of f_γ with (9).

Remark 2. One can easily see that the convergence in (6) holds pointwise and in the L^2-sense, if f is continuous and the support of the mollifier is contained in a ball whose radius tends to 0 as γ tends to 0. For a more precise characterization of the convergence see [10].

3.2. Positiveness of the solution

In some applications, inverse problems $Tf = g$ for probability densities f (with $T = R, C$) have to be solved, e.g. for the reconstruction of the directional distribution density f from its rose of intersection g for $T = C$. In this case, the numerical solution $\tilde{f}$ of $Tf = g$ has to satisfy the conditions $\int_{\mathscr{S}^{d-1}} \tilde{f}(\omega)\mathrm{d}\omega = 1$ and $\tilde{f} \geq 0$. The first condition can be always met by a simple renormalization. What about the positivity condition $\tilde{f} \geq 0$? If the data g is not contaminated by noise (i.e. exact) and we assume that we can integrate exactly, we get for all $\eta \in \mathscr{S}^{d-1}$ and $\gamma > 0$

$$f_\gamma(\eta) = \langle g, \psi_\gamma(\eta,\cdot)\rangle = \langle g, T^{-1}e_\gamma(\eta,\cdot)\rangle = \langle T^{-1}g, e_\gamma(\eta,\cdot)\rangle = \langle f, e_\gamma(\eta,\cdot)\rangle \geq 0,$$

because we consider only non-negative mollifiers $e_\gamma(\eta,\cdot)$.

If the data g is noisy, one can not guarantee the positiveness of $\tilde{f}$ anymore. However, in our numerical tests negative values of $\tilde{f}$ are spare and can be neglected, so a possibility to overcome this is to project $\tilde{f}$ onto the halfcone of non-negative functions after the reconstruction.

4. Inversion of the cosine transform in 2D

Since the calculation techniques for the reconstruction kernels differ in 2D and 3D, we consider the case $d = 2$ in this section separately.

The even functions on $\mathscr{S}^1$ correspond one-to-one to the π-periodic functions. Thus, to simplify the notation, in this section we consider densities w.r.t. the Lebesgue measure on the interval $[0,\pi]$. Notice the difference from the three-dimensional case, where we consider densities on the unit sphere w.r.t. the spherical surface area measure. In the two-dimensional case the cosine transform can be written in the form

$$C\varphi(x) = \int_0^\pi |\cos(x-t)|\varphi(t)\mathrm{d}t.$$

Furthermore it is in 2D closely related to the sine transform

$$S\varphi(x) = \int_0^\pi |\sin(x-t)|\varphi(t)\mathrm{d}t$$

by $C\varphi(x) = S\varphi(x+\pi/2)$. Thus, it suffices to consider the sine transform in the following which seems to be more common in the 2D case. The following Proposition (see [16, 17, 18]) enables us to calculate the reconstruction kernel.

Proposition 1. Let $g \in C^2(\mathbb{R})$ be an arbitrary π-periodic function. Then we have

$$Sf = g$$

with

$$f = \frac{1}{2}\left(g + g''\right).$$

Example. Let us consider the mollifier

$$e_\gamma(x,y) = \gamma^{-1} k_\nu \left(1 - \frac{(x-y)^2}{\gamma^2}\right)^\nu \mathbb{1}\{|x-y| \le \gamma\} \tag{10}$$

as a π-periodic function for $\nu \in \mathbb{N}$ and $\gamma \le \pi/2$ (see for example [19]), where

$$k_\nu^{-1} = \int_{-1}^{1} (1-x^2)^\nu \mathrm{d}x = \frac{\Gamma(\nu+1)\sqrt{\pi}}{\Gamma(\nu+\frac{3}{2})} \qquad (k_3^{-1} = \frac{32}{35},\ k_4^{-1} = \frac{256}{315}).$$

For $t = |x-y| < \gamma$ and $\nu \ge 3$ the reconstruction kernel is then calculated using Proposition 1:

$$\psi_\gamma(t) = \frac{k_\nu}{2\gamma}\left[\left(1-\frac{t^2}{\gamma^2}\right)^\nu + \frac{4t^2\nu(\nu-1)}{\gamma^4}\left(1-\frac{t^2}{\gamma^2}\right)^{\nu-2} - \frac{2\nu}{\gamma^2}\left(1-\frac{t^2}{\gamma^2}\right)^{\nu-1}\right].$$

5. Inversion of the spherical Radon and cosine transform in 3D

5.1. Reconstruction kernels for the spherical Radon transform in 3D

In this section we calculate reconstruction kernels for the spherical Radon transform. First of all we know that the spherical Radon transform commutes with rotations [4, Lemma C.2.7], i.e.

$$R(T_\rho f(\xi)) = T_\rho R f(\xi), \qquad \rho \in SO_3 \tag{11}$$

with $T_\rho f(\xi) := f(\rho^{-1}\xi)$. So it suffices to design the kernel for only one fixed reconstruction point $\eta \in \mathscr{S}^2$. We choose η as the north pole for this issue, and in this case the polar angle θ of a vector $\omega \in \mathscr{S}^2$ corresponds to the angle between η and ω. From now on we restrict our attention to mollifiers, which only depend on the geodesic distance $d_{\mathrm{geo}}(\eta,\omega) = \arccos(\langle\eta,\omega\rangle)$ and not on η and ω themselves. In other words, we consider only rotationally symmetric mollifiers, i.e. we have (by using spherical coordinates)

$$e_\gamma(\phi,\theta) = e_\gamma(\theta).$$

For such functions, the equation $Rf = g$ coincides with an Abel equation.

Theorem 2. [4, p. 432-434] Let $f, g \in C^1(\mathscr{S}^2)$ be rotationally symmetric functions with $Rf = g$. Then we have

$$\frac{2}{\pi}\int_0^x \frac{f(\arccos t)}{\sqrt{x^2-t^2}}\,\mathrm{d}t = g(\arcsin x), \quad 0 < x \le 1. \tag{12}$$

Define $G(x) := g(\arcsin x)$ and $F(t) := f(\arccos t)$, we get the Abel equation:

$$G(x) = \frac{2}{\pi}\int_0^x \frac{F(t)}{\sqrt{x^2-t^2}}\,\mathrm{d}t, \quad 0 < x \le 1. \tag{13}$$

This equation is solved by

$$F(t) = G(0) + t\int_0^t \frac{G'(x)}{\sqrt{t^2-x^2}}\,\mathrm{d}x, \quad 0 \le t \le 1, \tag{14}$$

with $F(0) = G(0)$, cf. [20, eq. 1.B.5ii].

Corollary 1. For a chosen C^1-smooth rotationally symmetric mollifier e_γ, the corresponding reconstruction kernel ψ_γ is therefore given by

$$\Psi_\gamma(t) = E_\gamma(0) + t \int_0^t \frac{E'_\gamma(\theta)}{\sqrt{t^2-\theta^2}}\,\mathrm{d}\theta, \tag{15}$$

with $\Psi_\gamma(t) = \psi_\gamma(\arccos t)$ and $E_\gamma(\theta) = e_\gamma(\arcsin\theta)$.

Of course one can evaluate (15) for any mollifier e_γ numerically via quadrature methods [20] or by the approximate inverse in order to determine the corresponding reconstruction kernel approximatively. However, for some special mollifiers, we are able to solve the equation analytically. We give two examples in following proposition.

Notice that we always require $\int_{\mathscr{S}^2} e_\gamma(\omega)\mathrm{d}\omega = 1$ for all $\gamma > 0$, see (7), which can be rewritten for rotationally symmetric mollifiers $e_\gamma(\theta)$ as

$$4\pi \int_0^{\pi/2} e_\gamma(\theta)\sin\theta \mathrm{d}\theta = 1 \quad \text{for all } \gamma > 0. \tag{16}$$

The function erfi is defined by $\mathrm{erfi} := -\mathrm{i}\,\mathrm{erf}(\mathrm{i}x)$, and erf denotes the well known error function $\mathrm{erf}(x) = 2/\sqrt{\pi}\int_0^x \exp(-t^2)\mathrm{d}t$.

Proposition 2. (i) Gaussian mollifier: Let

$$e_\gamma(\theta) = \frac{1}{c(\gamma)} \exp\left(-\frac{\sin^2\theta}{\gamma^2}\right), \quad \theta \in [0, \pi/2]$$

with normalizing constant

$$c(\gamma) = 2\,\pi^{3/2}\gamma \exp\left(-\gamma^{-2}\right) \mathrm{erfi}(1/\gamma)$$

originating from (16).

Then, the reconstruction kernel for the Radon transform in 3D is given by

$$\psi_\gamma(\theta) = \frac{1}{c(\gamma)}\left[1 - \frac{\sqrt{\pi}\cos\theta}{\gamma} \exp\left(-\frac{\cos^2\theta}{\gamma^2}\right) \mathrm{erfi}\left(\frac{\cos\theta}{\gamma}\right)\right].$$

(ii) Truncated polynomial: Let

$$e^1_\gamma(\theta) = \frac{1}{c_1(\gamma)} \begin{cases} 1 - \frac{\sin^2\theta}{\gamma^2}, & \theta \in [0, \arcsin(\gamma)], \\ 0, & \text{otherwise.} \end{cases}$$

with $c_1(\gamma) = 4\pi\left(1 + \frac{2}{3\gamma^2}(\sqrt{1-\gamma^2}-1) - \frac{2}{3}\sqrt{1-\gamma^2}\right)$.

Then, the reconstruction kernel for the Radon transform in 3D is

$$\psi^1_\gamma(\theta) = \frac{1}{c_1(\gamma)} \begin{cases} 1 - \frac{2\cos^2\theta}{\gamma^2}, & \text{if } \theta \geq \arccos(\gamma), \\ 1 - \frac{2\cos\theta}{\gamma^2}(\cos\theta - \sqrt{\cos^2\theta - \gamma^2}), & \text{if } \theta < \arccos(\gamma). \end{cases}$$

Proof. We shall show only (i). Calculations in case (ii) are done analogously.

With $E_\gamma(\theta) = e_\gamma(\arcsin\theta) = \frac{1}{c(\gamma)}\exp\left(-\theta^2/\gamma^2\right)$ (15) yields

$$\begin{aligned} \Psi_\gamma(t) &= E_\gamma(0) + t\int_0^t \frac{E'_\gamma(x)}{\sqrt{t^2-x^2}}\,\mathrm{d}x \\ &= \frac{1}{c(\gamma)}\left(1 - \frac{t}{\gamma^2}\int_0^t \frac{2x\exp\left(-x^2/\gamma^2\right)}{\sqrt{t^2-x^2}}\,\mathrm{d}x\right). \end{aligned}$$

Since

$$\int_0^t \frac{2x\exp\left(-x^2/\gamma^2\right)}{\sqrt{t^2-x^2}}\,\mathrm{d}x = \sqrt{\pi}\gamma\exp\left(-t^2/\gamma^2\right)\operatorname{erfi}\left(t/\gamma\right),$$

which follows by the substitution $y=\sqrt{t^2-x^2}$ and from the integration formula

$$\int \exp\left(z^2/\gamma^2\right)\mathrm{d}z = \frac{\sqrt{\pi\gamma^2}}{2}\operatorname{erfi}\left(z/\gamma\right)$$

(see [21, equation 2.33]), we obtain the reconstruction kernel

$$\psi_\gamma(\theta) = \Psi_\gamma(\cos\theta) = \frac{1}{c(\gamma)}\left[1-\frac{\sqrt{\pi}\cos\theta}{\gamma}\exp\left(-\frac{\cos^2\theta}{\gamma^2}\right)\operatorname{erfi}\left(\frac{\cos\theta}{\gamma}\right)\right].$$

□

Remark 3. For $\nu \geq 2$ the calculation of the corresponding reconstruction kernels for mollifiers

$$e_\gamma^\nu(\theta) = \frac{1}{c_\nu(\gamma)}\begin{cases} \left(1-\frac{\sin^2\theta}{\gamma^2}\right)^\nu, & \theta\in[0,\arcsin(\gamma)],\\ 0, & \text{otherwise}\end{cases}$$

can be done analogously.

5.2. Reconstruction kernel for the cosine transform in 3D

Proposition 3. Let $\psi_\gamma(\theta)$ be the rotationally symmetric reconstruction kernel for the Radon transform in 3D for the mollifier $e_\gamma(\theta)$, which lies in the range of the cosine transform. Then, the reconstruction kernel for the cosine transform for the same mollifier is given by

$$\overline{\psi}_\gamma(\theta) = \frac{1}{4\pi}\left(\frac{\cos\theta}{\sin\theta}\psi_\gamma'(\theta)+\psi_\gamma''(\theta)+2\psi_\gamma(\theta)\right), \quad \theta\in[0,\pi/2].$$

Proof. For a rotationally symmetric function f the block operator (2) can be calculated by

$$\Box f = \frac{1}{4\pi}\left(\frac{\cos\theta}{\sin\theta}\frac{\partial f}{\partial\theta}+\frac{\partial^2 f}{\partial\theta^2}+2f\right). \tag{17}$$

Furthermore, the following equality holds (see [6])

$$\Box R^{-1} = R^{-1}\Box = C^{-1}$$

which can be seen using spherical harmonics. Now let $\overline{\psi}_\gamma$ be the reconstruction kernel for the cosine transform and ψ_γ be the kernel for the Radon transform for the same mollifier e_γ, then $C\overline{\psi}_\gamma = e_\gamma$ is equivalent to

$$\overline{\psi}_\gamma = C^{-1}e_\gamma = \Box R^{-1}e_\gamma = \Box\Psi_\gamma.$$

□

In case of the Gaussian mollifier, the corresponding kernel can be written as

$$\overline{\psi}_\gamma(\theta) = \frac{1}{2\pi\gamma^5 c(\gamma)} \left[\sqrt{\pi} \exp\left(\frac{-\cos^2\theta}{\gamma^2}\right) \operatorname{erfi}\left(\frac{\cos\theta}{\gamma}\right) \cos\theta \cdot T_1 + T_2 \right] + (2\pi)^{-1}$$

with

$$T_1 = 3\gamma^2 - 5\gamma^2\cos^2\theta - 2\cos^2\theta + 2\cos^4\theta,$$
$$T_2 = 2\gamma(\cos^2\theta)(1 - \cos^2\theta + 2\gamma^2) - \gamma^2.$$

6. Regularization

In this section, we characterize mollifiers, which lead to regularizations. In particular, we show that the mollifiers introduced in Section 5 fulfil these conditions.

We denote by T^+ the generalized inverse of the operator T, where T is the spherical Radon transform R or the cosine transform C. Let $g = Tf$ be the transform of f, $g^\varepsilon := g + \delta_\varepsilon$ for some noise δ_ε with $\|\delta_\varepsilon\| \leq \varepsilon$ and T_γ as in (9). The error of the reconstruction of f from the data g^ε can be estimated from above using the triangle inequality as follows:

$$E_{\text{total}} := \|T_\gamma g^\varepsilon - T^+ g\| \leq \|T_\gamma g^\varepsilon - T_\gamma g\| + \|T_\gamma g - T^+ g\| = E_{\text{data}} + E_{\text{appr}}, \quad (18)$$

where E_{data} represents the error of the data, i.e. the error resulting from adding ε. The error caused by the approximation T_γ is represented by E_{appr}. See [19, Th. 2.4] for an upper bound for the data error.

Definition 1. A regularization of T^+ for finding the solution f of $Tf = g$ is a family of operators $\{T_\gamma\}_{\gamma>0}$ with a mapping $\gamma : \mathbb{R}^+ \times L^2(\mathscr{S}^2) \to \mathbb{R}^+$, such that for all $g \in D(T^+)$ and for all g^ε with $\|g - g^\varepsilon\| \leq \varepsilon$ the equality

$$\lim_{\varepsilon\to 0, g^\varepsilon \to g} T_{\gamma(\varepsilon, g^\varepsilon)} g^\varepsilon = T^+ g$$

holds (in the L^2-sense), and thus, E_{total} goes to 0 as ε goes to 0.

In order to show that our method leads to a regularization, we want to apply the following theorem from [22] which provides a suitable characterization of regularizations in the setting of Sobolev spaces. For both transforms under consideration, we have the norm inequality

$$a\|f\|_{H^{-\alpha}} \;\leq\; \|Tf\|_{L^2} \;\leq\; a^{-1}\|f\|_{H^{-\alpha}} \quad (19)$$

with constants $a > 0$ and α which depend on the dimension d (cf. (5)).

Theorem 3. Let $M_\gamma : H^{-\alpha} \to L^2$ be a family of linear continuous operators such that

$$(i) \quad \|M_\gamma f\|_{L^2} \leq k(\gamma)\|f\|_{H^{-\alpha}}, \qquad f \in N(T)^\perp$$
$$(ii) \quad \lim_{\gamma\to 0} \|M_\gamma f - f\|_{L^2} = 0, \qquad f \in N(T)^\perp$$
$$(iii) \quad k(\gamma)\varepsilon \to 0 \quad \text{for} \quad \varepsilon, \gamma \to 0,$$

where $N(T)$ is the null space of the operator T. Then $T_\gamma = M_\gamma T^+$ is a regularization of T^+ for finding f.

Here, condition (i) is equivalent to the convergence to 0 of the data error, and (ii) to the convergence of the approximation error.

6.1. Two-dimensional case

First, we analyze the two-dimensional case. As in Section 4, we consider π-periodic functions to simplify the notation. For our calculations we introduce the family $\left\{ b_k(\cdot) := \frac{1}{\sqrt{\pi}} \exp(2ik\cdot), k \in \mathbb{Z} \right\}$, which is an orthonormal basis of $L^2[-\pi/2, \pi/2]$. Therefore we have for $f \in L^2[-\pi/2, \pi/2]$

$$\lim_{N\to\infty} \left\| f - \sum_{k=-N}^{N} \hat{f}_k b_k \right\|_{L^2[-\pi/2,\pi/2]} = 0,$$

where

$$\hat{f}_k = \int_{-\pi/2}^{\pi/2} f(t) b_k(t) \mathrm{d}t.$$

The Parseval identity reads

$$\|f\|^2_{L^2[-\pi/2,\pi/2]} = \int_{-\pi/2}^{\pi/2} f(t)^2 \mathrm{d}t = \sum_{k=-\infty}^{\infty} |\widehat{f}_k|^2.$$

The Sobolev space $H^\alpha[-\pi/2, \pi/2]$, $0 \le \alpha < \infty$ is the space of all functions $f \in L^2[-\pi/2, \pi/2]$ with

$$\sum_{k=-\infty}^{\infty} \left(k^2+1\right)^\alpha |\widehat{f}_k|^2 < \infty. \tag{20}$$

By $H^{-\alpha}[-\pi/2, \pi/2]$ we denote the dual space of $H^\alpha[-\pi/2, \pi/2]$, where the norm is also given by (20) when the exponent α is replaced by $-\alpha$ (see [23, Chapter 8]). The convolution of two π-periodic functions is given by $(f * g)(x) = \int_{-\pi/2}^{\pi/2} f(t) g(x-t) \mathrm{d}t$. In the following we consider mollifiers e_γ, $\gamma \le \pi/2$ of the form $e_\gamma(t) = \gamma^{-1} e(t/\gamma)$, continuated as a π-periodic function, where e is a non-negative smooth function with support in [-1,1] and $\int_{-1}^{1} e(t)\mathrm{d}t = 1$.

One example is the function from Section 4

$$e(t) = k_\nu \left(1-t^2\right)^\nu \mathbb{1}\{t \le 1\} \qquad \text{with} \qquad k_\nu^{-1} = \int_{-1}^{1} \left(1-x^2\right)^\nu \mathrm{d}x.$$

Theorem 4. Let e_γ be of the above type, where e is in $H^\alpha[-\pi/2, \pi/2]$. Then

$$\begin{aligned} &(i) \quad \|e_\gamma * f\|_{L^2[-\pi/2,\pi/2]} \le k(\gamma) \|f\|_{H^{-\alpha}[-\pi/2,\pi/2]}, \quad && f \in L^2[-\pi/2, \pi/2], \\ &(ii) \quad \lim_{\gamma\to 0} \|e_\gamma * f - f\|_{L^2[-\pi/2,\pi/2]} = 0, && f \in L^2[-\pi/2, \pi/2]. \end{aligned}$$

If $k(\gamma)\varepsilon \to 0$ for $\varepsilon, \gamma \to 0$, then $T_\gamma g = e_\gamma * T^+ g$ is a regularization for T^+.

Proof. With the convolution theorem, i.e. $\widehat{(f*g)}_k = \widehat{f}_k \widehat{g}_k$ we get

$$\begin{aligned} \|e_\gamma * f\|^2_{L^2[-\pi/2,\pi/2]} &= \sum_{k=-\infty}^{\infty} |\widehat{(e_\gamma * f)}_k|^2 \\ &= \sum_{k=-\infty}^{\infty} |(\widehat{e_\gamma})_k|^2 |\widehat{f}_k|^2 \\ &= \sum_{k=-\infty}^{\infty} \left(k^2+1\right)^\alpha |(\widehat{e_\gamma})_k|^2 \left(k^2+1\right)^{-\alpha} |\widehat{f}_k|^2 \\ &\le \sup_{k\in Z} \left\{ \left(k^2+1\right)^\alpha |(\widehat{e_\gamma})_k|^2 \right\} \|f\|^2_{H^{-\alpha}[-\pi/2,\pi/2]}. \end{aligned}$$

Combined with

$$k(\gamma)^2 := \sup_{k\in Z}\left\{\left(k^2+1\right)^{\alpha}|(\widehat{e_\gamma})_k|^2\right\} \le \sum_{k=-\infty}^{\infty}\left(k^2+1\right)^{\alpha}|(\widehat{e_\gamma})_k|^2 = \|e_\gamma\|^2_{H^\alpha[-\pi/2,\pi/2]} < \infty$$

this proves (i). Furthermore, for $\gamma \le \pi/2$ we use the substitution $z = t/\gamma$ to arrive at

$$\begin{aligned}
\|f - e_\gamma * f\|^2_{L^2[-\pi/2,\pi/2]} &= \int_{-\pi/2}^{\pi/2}\left(f(x) - \int_{-\pi/2}^{\pi/2} f(x-t)e_\gamma(t)\mathrm{d}t\right)^2 \mathrm{d}x \\
&= \int_{-\pi/2}^{\pi/2}\left(\int_{-\pi/2}^{\pi/2}[f(x)-f(x-t)]\gamma^{-1}e\left(t/\gamma\right)\mathrm{d}t\right)^2 \mathrm{d}x \\
&= \int_{-\pi/2}^{\pi/2}\left(\int_{-1}^{1}[f(x)-f(x-\gamma z)]\sqrt{e(z)}\sqrt{e(z)}\mathrm{d}z\right)^2 \mathrm{d}x \\
&\le \int_{-\pi/2}^{\pi/2}\left(\left(\int_{-1}^{1}[f(x)-f(x-\gamma z)]^2 e(z)\mathrm{d}z\right)^{\frac{1}{2}}\left(\int_{-1}^{1}e(z)\mathrm{d}z\right)^{\frac{1}{2}}\right)^2 \mathrm{d}x \\
&= \int_{-\pi/2}^{\pi/2}\int_{-1}^{1}[f(x)-f(x-\gamma z)]^2 e(z)\mathrm{d}z\,\mathrm{d}x \\
&= \int_{-1}^{1}\|f(\cdot)-f(\cdot-\gamma z)\|^2_{L^2[-\pi/2,\pi/2]}\,e(z)\mathrm{d}z,
\end{aligned}$$

where we have used that the support of e is in $[-1,1]$. Since $\|f(\cdot)-f(\cdot-\gamma z)\|_{L^2[-\pi/2,\pi/2]} \le 2\|f\|_{L^2[-\pi/2,\pi/2]}$ and $\|f(\cdot)-f(\cdot-\gamma z)\|^2_{L^2[-\pi/2,\pi/2]}$ goes to zero for all $z\in[-1,1]$ as $\gamma\to 0$ (see [24, Theorem 5.21]), Lebesgue's theorem yields property (ii).

The application of Theorem 4 finishes the proof. □

Since $\alpha = 2$ for the cosine transform in $2D$, the choice of ν greater than three in (10) leads to $e \in H^\alpha[-\pi/2,\pi/2]$ and thus guarantees that our method leads to a regularization.

6.2. Three-dimensional case

To derive a regularization for our estimator, we define the operator M_γ in Theorem 3 as the spherical convolution

$$M_\gamma f(x) = (e_\gamma * f)(x) := \int_{\mathscr{S}^2} e_\gamma(\langle x,y\rangle)f(y)\mathrm{d}y,$$

where we assume that the mollifier e_γ is even, continuous and non-negative, which means that $e_\gamma * f$ is even as well.

First we analyze the data error. For this purpose, we need the notion of the Legendre coefficients of a function $g\in L^2[-1,1]$ which are defined as

$$L_n g := 2\pi\langle g, P_n\rangle_{L^2[-1,1]} = 2\pi\int_{-1}^{1} g(t)P_n(t)\mathrm{d}t, \quad n\in\mathbb{N}, \tag{21}$$

where $\{P_n\}_{n\in\mathbb{N}}$ are the Legendre polynomials on $[-1,1]$, see e.g. [5].

For $g \in L^2[-1,1]$ it holds that ([25, p. 116])

$$\lim_{N\to\infty} \left\| g - \sum_{n=0}^{N} \frac{2n+1}{4\pi} (L_n g) P_n \right\|_{L^2([-1,1])} = 0,$$

which is equivalent to the Parseval identity

$$\|g\|^2_{L^2[-1,1]} = \sum_{n=0}^{\infty} \frac{2n+1}{4\pi} (L_n g)^2 < \infty.$$

Using polar coordinates $(x,y,z) = (\sqrt{1-t^2}\cos\phi, \sqrt{1-t^2}\sin\phi, t), 0 \le \phi \le 2\pi, -1 \le t \le 1$, the 'longitude-independent' part of the Beltrami Laplace Operator is given by (see [25, p. 116])

$$D_t = \tfrac{\partial}{\partial t}(1-t^2)\tfrac{\partial}{\partial t} = -2t\tfrac{\partial}{\partial t} + (1-t^2)\tfrac{\partial^2}{\partial t^2}.$$

For the Legendre polynomials we have (see [5, 25])

$$D_t P_n(t) = -n(n+1)P_n(t), \qquad t \in [-1,1]$$

and it is not difficult to see that the operator D_t is selfadjoint w.r.t. the L^2-inner product. Thus, for a function $g \in C^{2l}[-1,1]$ it holds

$$\begin{aligned}\left(L_n(D_t^l g)\right)^2 &= \left(2\pi \int_{-1}^{1} D_t^l g(t) P_n(t) \mathrm{d}t\right)^2 = \left(2\pi \int_{-1}^{1} g(t) D_t^l P_n(t) \mathrm{d}t\right)^2 \\ &= n^{2l}(n+1)^{2l} \left(2\pi \int_{-1}^{1} g(t) P_n(t) \mathrm{d}t\right)^2 = n^{2l}(n+1)^{2l} (L_n g)^2\end{aligned}$$

and therefore for fixed l

$$\begin{aligned}\infty > 2^{2l-1}\|D_t^l g\|^2_{L^2[-1,1]} &= 2^{2l-1} \sum_{n=0}^{\infty} \frac{2n+1}{4\pi} \left(L_n D_t^l g\right)^2 \qquad (22)\\ &= (4\pi)^{-1} \sum_{n=0}^{\infty} 2^{2l-1}(2n+1)n^{2l}(n+1)^{2l} (L_n g)^2 \\ &\ge (4\pi)^{-1} \max_{n\ge 0} \left\{ (2n^2)^{2l} (L_n g)^2 \right\} \ge (4\pi)^{-1} \max_{n\ge 1} \left\{ \left(n^2+1\right)^{2l} (L_n g)^2 \right\}\end{aligned}$$

since all sumands are positive.

Lemma 1. Let $e_\gamma \in C^{2l}_{\mathrm{e}}[-1,1]$, $\gamma > 0$, $l \in \mathbb{N}$ with $2\pi\|e_\gamma\|_{L^1[-1,1]} = 1$ and $f \in L^2(\mathscr{S}^2)$. Then there is a constant $\tilde{c} = \tilde{c}(e_\gamma)$ such that

$$\|e_\gamma * f\|_{L^2(\mathscr{S}^2)} \le \tilde{c}\|f\|_{H^{-2l}}.$$

Proof. Using the Funk-Hecke-Theorem ([5, 25]), we have for spherical harmonics Y_{nk}

$$\begin{aligned}\langle e_\gamma * f, Y_{nk}\rangle &= \int_{\mathscr{S}^2}\int_{\mathscr{S}^2} e_\gamma(\langle x,y\rangle) f(y)\mathrm{d}y Y_{nk}(x)\mathrm{d}x \\ &= \int_{\mathscr{S}^2} \left(\int_{\mathscr{S}^2} e_\gamma(\langle x,y\rangle) Y_{nk}(x)\mathrm{d}x \right) f(y)\mathrm{d}y \\ &= \int_{\mathscr{S}^2} 2\pi (L_n e_\gamma) Y_{nk}(y) f(y)\mathrm{d}y \\ &= 2\pi (L_n e_\gamma)\langle f, Y_{nk}\rangle.\end{aligned}$$

Finally we get using Hölder's inequality

$$\begin{aligned}\|e_\gamma * f\|^2_{L^2(\mathscr{S}^2)} &= \sum_{n \text{ even}} \sum_{k=1}^{2n+1} \langle e_\gamma * f, Y_{nk}\rangle^2 \\ &= 4\pi^2 \sum_{n \text{ even}} \left((L_n e_\gamma)^2 \left(n^2+1\right)^{2l} \left(n^2+1\right)^{-2l} \sum_{k=1}^{2n+1} \langle f, Y_{nk}\rangle^2 \right) \\ &\leq \tilde{c} \sum_{n \text{ even}} \left(n^2+1\right)^{-2l} \sum_{k=1}^{2n+1} \langle f, Y_{nk}\rangle^2 \\ &\leq \tilde{c}\, \|f\|_{H^{-2l}},\end{aligned}$$

where $\tilde{c}(\gamma) = 4\pi^2 \max_{n\geq 0} \left\{ \left(n^2+1\right)^{2l} \left(L_n e_\gamma\right)^2 \right\}$. Since $e_\gamma \in C^{2l}_{\mathrm{e}}$ for all γ, we know from (22) that

$$\tilde{c}(\gamma) \leq \max \left\{ 2^{2l+3}\pi^3 \|D^l_t e_\gamma\|^2_{L^2[-1,1]}, 4\pi^2 \right\} < \infty,$$

because $L_0 e_\gamma \leq 2\pi \|e_\gamma\|_{L^1[-1,1]} = 1$. □

Next we analyze the approximation error.

Lemma 2. Let e_γ be an even continuous non-negative function with $2\pi \int_{-1}^{1} e_\gamma(t)\mathrm{d}t = 1$. Then the following statements are equivalent:

$$\begin{aligned}&(i) \quad \lim_{\gamma\to 0} \|e_\gamma * f - f\|_{L^2(\mathscr{S}^2)} = 0, \quad f \in L^2_{\mathrm{e}}(\mathscr{S}^2) \\ &(ii) \quad \lim_{\gamma\to 0} L_{2n} e_\gamma = 1, \quad n \in \mathbb{N} \\ &(iii) \quad \lim_{\gamma\to 0} \int_0^\rho e_\gamma(t)\mathrm{d}t = 0, \quad \rho \in [0,1)\end{aligned}$$

Proof. The equivalence of (i) and (ii) can be shown analogously to the proof of Theorem 3.2 in [26]. The rest of the proof follows ideas presented in [25].

$(ii) \to (iii)$

Since e_γ is non-negative, the following inequality holds (note $P_2(t) = \frac{1}{2}(3t^2-1)$)

$$\begin{aligned}0 \leq \int_0^\rho e_\gamma(t)\mathrm{d}t \leq \int_{-\rho}^{\rho} e_\gamma(t)\mathrm{d}t &\leq \frac{1}{\frac{3}{2}(1-\rho^2)} \int_{-\rho}^{\rho} \tfrac{3}{2}(1-t^2) e_\gamma(t)\mathrm{d}t \\ \leq \frac{1}{\frac{3}{2}(1-\rho^2)} \int_{-1}^{1} \left[1 - \tfrac{1}{2}(3t^2-1)\right] e_\gamma(t)\mathrm{d}t &\leq \frac{1}{3\pi(1-\rho^2)} (L_0 e_\gamma - L_2 e_\gamma)\end{aligned}$$

and the right hand side converges to zero due to (ii).

$(iii) \to (ii)$

We show that for all $\varepsilon > 0$ and $n \in \mathbb{N}$ the inequality

$$1 - \varepsilon \leq \lim_{\gamma\to 0} L_{2n} e_\gamma \leq 1$$

holds. The upper bound $L_{2n} e_\gamma \leq 1$ clearly holds, since $|P_n(t)| \leq 1$ for $t \in [-1,1]$. Because of $P_{2n}(1) = 1$, there exists some δ with

$$P_{2n}(t) \geq \sqrt{1-\varepsilon/2}, \qquad t \in (\delta, 1].$$

With $\rho = \delta$ property (iii) implies that for some γ_1

$$\left| 4\pi \int_0^\delta e_\gamma(t) \mathrm{d}t \right| \leq \varepsilon/2, \qquad \gamma \leq \gamma_1$$

and therefore the inequality

$$4\pi \int_0^\delta e_\gamma(t) P_{2n}(t) \mathrm{d}t \geq -4\pi \int_0^\delta e_\gamma(t) \mathrm{d}t \geq -\varepsilon/2, \qquad \gamma \leq \gamma_1$$

holds. Since using again property (iii) leads to

$$\frac{1}{2\pi} = \lim_{\gamma \to 0} \int_{-1}^1 e_\gamma(t) \mathrm{d}t = 2 \lim_{\gamma \to 0} \int_\delta^1 e_\gamma(t) \mathrm{d}t$$

we have for all $\gamma \leq \gamma_2$:

$$4\pi \int_\delta^1 e_\gamma(t) \mathrm{d}t \geq \sqrt{1 - \varepsilon/2}.$$

It follows for $\gamma \leq \min\{\gamma_1, \gamma_2\}$:

$$\begin{aligned} L_{2n} e_\gamma &= 4\pi \left(\int_0^\delta e_\gamma(t) P_{2n}(t) \mathrm{d}t + \int_\delta^1 e_\gamma(t) P_{2n}(t) \mathrm{d}t \right) \\ &\geq 4\pi \left(\int_0^\delta e_\gamma(t) P_{2n}(t) \mathrm{d}t + \sqrt{1 - \varepsilon/2} \int_\delta^1 e_\gamma(t) \mathrm{d}t \right) \\ &\geq -\varepsilon/2 + 1 - \varepsilon/2 \\ &\geq 1 - \varepsilon \end{aligned}$$ □

Combining the results of Theorem 3 and Lemma 1 and 2 we get the following theorem.

Theorem 5. Let $M_\gamma f = (e_\gamma * f)(x)$ be a spherical convolution such that

(i) $\quad e_\gamma \in C_{\mathrm{e}}^{2l}[-1,1]$ for some $l \in \mathbb{N}$ with $2l \geq \alpha$

(ii) $\quad \lim_{\gamma \to 0} \int_0^\rho e_\gamma(t) \mathrm{d}t = 0, \qquad \rho \in [0,1)$

(iii) $\quad \tilde{c}(\gamma)\varepsilon \to 0$ for $\varepsilon, \gamma \to 0$

with $\tilde{c}(\gamma) = 4\pi^2 \max_{n \geq 0} \left\{ \left(n^2+1\right)^{2l} \left(L_n e_\gamma\right)^2 \right\}$ as in Lemma 1. Then $T_\gamma = M_\gamma T^+$ is a regularization of T^+.

Consider the examples of mollifiers from Section 5 in polar coordinates:

(a) $\tilde{e}_\gamma(t) = \frac{1}{c_\nu(\gamma)} \begin{cases} \left(1 - \frac{1-t^2}{\gamma^2}\right)^\nu, & t \in [\sqrt{1-\gamma^2}, 1], \\ 0, & \text{otherwise}, \end{cases}$
with $\nu \in \mathbb{N}$ and $c_\nu(\gamma)$, such that $2\pi \|e_\gamma\|_{L^1[-1,1]} = 1$,

(b) $\tilde{e}_\gamma(t) = \frac{1}{c(\gamma)} \exp\left(-\frac{1-t^2}{\gamma^2}\right)$,
with $c(\gamma) = 2\,\pi^{3/2} \gamma \exp\left(-\gamma^{-2}\right) \operatorname{erfi}(1/\gamma)$.

Both mollifiers are non-negative and have by construction the property

$$1 = 2\pi\|e_\gamma\|_{L^1[-1,1]} = 2\pi\int_{-1}^{1}|e_\gamma(t)|\mathrm{d}t = \int_{\mathscr{S}^2} e_\gamma(\langle x,y\rangle)\mathrm{d}y.$$

For the spherical Radon transform (19) is fulfilled for $\alpha = \frac{1}{2}$ and in case of the cosine transform for $\alpha = \frac{5}{2}$, therefore we get the following corollary.

Corollary 2. Both mollifiers lead to a regularization for the spherical Radon transform. For the cosine transform only those, which lie in $C^4[-1,1]$, i.e. all mollifiers of type (a) with $\nu \geq 4$ and all mollifiers of type (b).

Proof. We only have to show property (ii) of the last theorem for these mollifiers. For type (a) this is clear because it has limited support. For type (b) the result follows using L'Hospital. For $\rho \in [0,1)$ we have

$$\begin{aligned}\lim_{\gamma\to 0}\int_0^\rho e_\gamma(t)\mathrm{d}t &= \lim_{\gamma\to 0}\frac{1}{c(\gamma)}\int_0^\rho \exp\left(-\frac{1-t^2}{\gamma^2}\right)\mathrm{d}t \\ &= \lim_{\gamma\to 0}\frac{\int_0^\rho \exp\left(-\frac{1-t^2}{\gamma^2}\right)\mathrm{d}t}{4\pi\int_0^1 \exp\left(-\frac{1-t^2}{\gamma^2}\right)\mathrm{d}t} = \lim_{\gamma\to 0}\frac{\int_0^{\rho/\gamma}\exp\left(y^2\right)\mathrm{d}y}{4\pi\int_0^{1/\gamma}\exp\left(y^2\right)\mathrm{d}y} \\ &\overset{L'H.}{=} (4\pi)^{-1}\lim_{\gamma\to 0}\frac{\frac{-\rho}{\gamma^2}\exp\left(\left(\frac{\rho}{\gamma}\right)^2\right)}{\frac{-1}{\gamma^2}\exp\left(\frac{1}{\gamma^2}\right)} = (4\pi)^{-1}\lim_{\gamma\to 0}\rho\exp\left(\frac{1}{\gamma^2}(\rho^2-1)\right) = 0.\end{aligned}$$

□

7. Numerical experiments with synthetic data

In this section we present some numerical tests. We mostly use cylinder processes which can be introduced as follows. We denote by a cylinder a line dilated with a ball of a certain radius. The *directional distribution* of a stationary cylinder process is the distribution of the direction of a typical cylinder. The *intensity* of a cylinder process is the mean total length of the underlying line process in a unit volume. For a rigorous definition of cylinder processes and their directional distribution see [27] or [28].

As already mentioned in the introduction, it is a well-known approach to estimate the directional distribution of a cylinder process by counting intersections with test planes and applying an inversion of the cosine transform to retrieve the directional distribution. In the following we perform numerical simulations and apply the method introduced in this paper to the data. We also apply other approaches and compare the results.

7.1. Inversion of the cosine transform in 2D

For the 2D case, we compare our approach to other methods for the estimation of the directional distribution, namely a Fourier method as described in [29] and a method suggested by Digabel (see [30]). An overview of such estimators can be found in [31]. For our tests we

assume that we can access the data, i.e. the estimation of the rose of intersections, at the angles $\frac{n\pi}{100}$, $n = 0,\dots 99$, and use the same points to evaluate the results. For all reconstructions, we use the same parameters. Depending on the degree of distortion resulting from the estimation of the cosine transform of the density, the smoothing is sometimes a little too much or too less. For our approach we use the polynomial kernel with parameters $\nu = 5$ and $\gamma = 0.4$. The parameter for Digabel's method has been chosen such that the results are similar to the ones of our approach.

A first analysis (see Figure 2) shows the results of the methods applied to a theoretical cosine transform of a density, in this case a mixture of a von Mises and a beta distribution. The von Mises density on the interval $[0,2\pi)$ is defined as $f_{\mathrm{vM}}(x) = \frac{\exp(\kappa\cos(x-\mu))}{2\pi I_0(\kappa)}$, for $\mu \in [0,2\pi)$, $\kappa > 0$, where I_0 is the modified Bessel function of order zero. Thus, the function $\tilde{f}_{\mathrm{vM}}(x) = f_{\mathrm{vM}}(x) + f_{\mathrm{vM}}(x+\pi)$ is a probability density on $[0,\pi)$. The beta density on $[0,1]$ is defined as $f_\beta(x) = \frac{1}{B(\alpha,\beta)} x^{\alpha-1}(1-x)^{\beta-1}$, where $\alpha,\beta > 0$, and B is the beta function. To get a density function on $[0,\pi)$ we have simply rescaled it accordingly. For the density presented here, we chose the parameters $\kappa = 10$, $\mu = 1$ for the von Mises distribution, and $\alpha = 2$, $\beta = 10$ for the beta distribution, respectively.

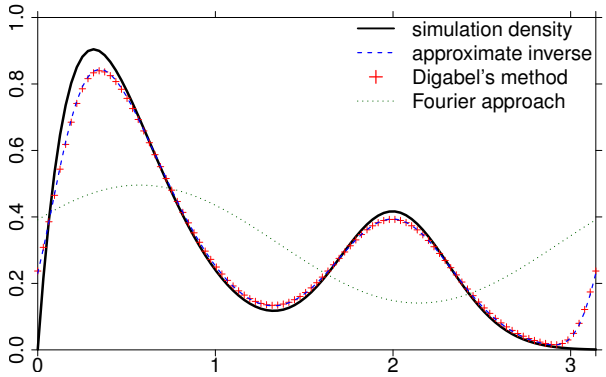

Figure 2. Comparison of the three reconstruction methods on theoretical data

In our first simulation study we simulate a line process in the unit ball with intensity 10000 and count the intersections with the set of test lines analytically. For each direction we consider only one test line, namely the one through the origin, which produces highly distorted data. The results can be found in Figure 3.

For our second simulation study we have considered cylinder processes with radius 3 and intensity 25 in the unit square. These processes have been voxelized with a resolution of 1000 x 1000 pixels, i.e. a cylinder is 6 pixels thick. Then, the images are skeletonized using the software Avizo which produces a set of line segments as result. Using this set we have estimated the rose of intersections taking an average over 10 simulations. Since the intensity is always underestimated considerably we renormalized the graphs to get a valid density function. The results are depicted in Figure 4.

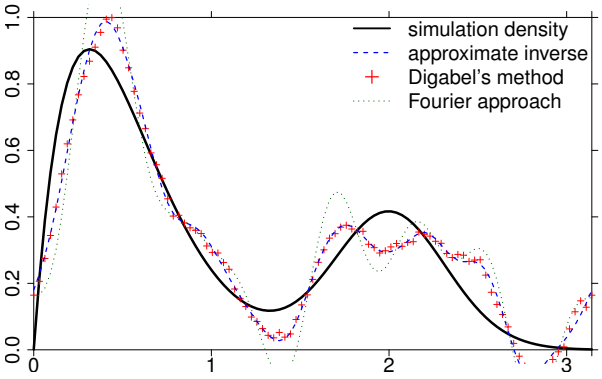

Figure 3. Comparison of the methods on simulated data in the unit ball, intersections counted analytically

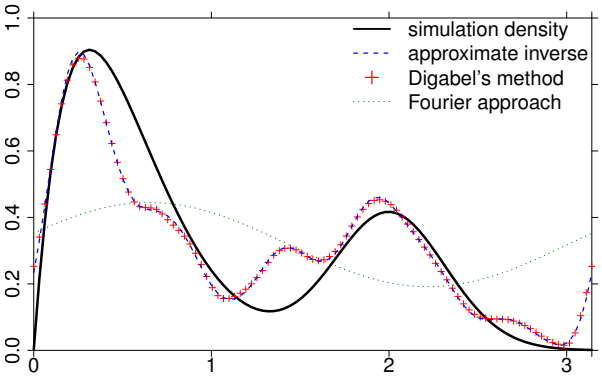

Figure 4. Comparison of the methods on simulated voxel data in the unit square, intersections counting based on skeletonization

7.2. Numerical integration on the sphere $\mathscr{S}^2$

In this section, we turn to the three-dimensional case, where a numerical integration over $\mathscr{S}^2$ is necessary, since only discrete values of g are available in applications. Thus, in order to use the approximate inverse, we need a discretization of the integral

$$\langle g, \psi_\gamma(\eta,\cdot)\rangle_{L^2(\mathscr{S}^{d-1})} = \int_{\mathscr{S}^2} g(\omega)\psi_\gamma(\eta,\omega)\mathrm{d}\omega. \tag{23}$$

This integrand is an even function, so is suffices to integrate over the positive hemisphere. The best known integration formulas over the sphere are the product formulas. They can be easily modified to integrate only over the positive hemisphere and they have invariances for rotations along the z-axis, which leads to reduction of storage for the reconstruction kernel. But on the other hand these rules on the sphere have the disadvantage, that the points are badly geometrically distributed (the points cluster at the poles) and the meshes are of different size and shape.

To overcome this problem, there are many approaches in the literature. Well-known examples are the so-called spherical t-designs [32] or the cubature formulae from Fliege and Maier [33]. But here we will use the integration technique called extremal systems of points on the sphere for the integration [34]. Approximations for these point sets and

the corresponding integration weights can be found at the page `http://web.maths.unsw.edu.au/~rsw/Sphere/Extremal/New/index.html`. These point sets are designed for integration over the whole sphere. Unfortunately, they are not symmetric w.r.t. the origin, so we can't easily take advantage of the fact that our integrand is an even function. This problem should be investigated in the future.

Remark 4. Since the reconstruction kernel is analytically given on the whole sphere and it has only small support, it is possible to stabilize the integration by creating artificial data points g (for example by a kernel smoother with a uniform or an exponential kernel) and use an integration formula with more points.

7.3. Inversion of the spherical Radon transform in 3D

Figure 5 shows the reconstruction kernels as functions of the polar angle θ for the Gaussian mollifier. In the following we use 900 points of the corresponding transform to calculate our reconstructions.

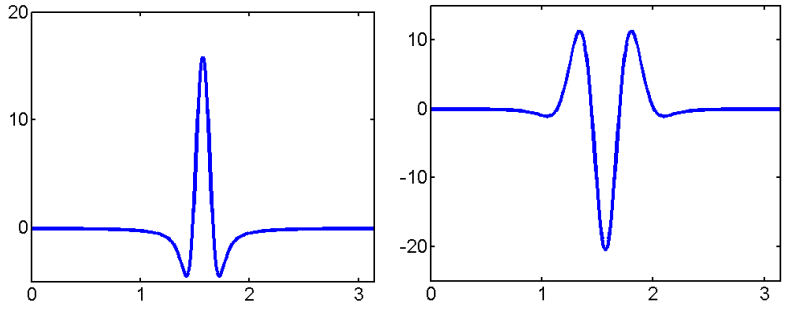

(a) Spherical Radon transform ($\gamma = 0.1$)

(b) Cosine transform ($\gamma = 0.22$)

Figure 5. Reconstruction kernels for the Gaussian mollifier as functions of the polar angle

We use synthetic data to illustrate the results of our numerical inversion algorithm for the spherical Radon transform. We consider the function

$$f(x,y,z) = \cos(3\pi(z-y)) + \cos(3\pi x),$$

see Figure 6(a). In Figure 6, the reconstructions from the values of the Radon transform (Figure 6(d)) are given. In this section we use the same colour map in these figures as for the function itself. Both reconstruction kernels lead to good results, but the reconstruction with the Gaussian kernel is smoother and works a little bit better in this example. One can see in the plots that some of the values, especially in regions with high jumps, are too small.

Now we perturb the Radon transform of f with normal noise, i.e. we add a centred, rotation invariant Gaussian random field X with continuous covariance function and $\mathrm{Cov}(X(t_1),X(t_2)) = 0$ for all $d_{\mathrm{geo}}(t_1,t_2) > r$, where we choose r to be small enough such that the values of the field at two arbitrary measurement points are uncorrelated. The (constant) standard deviation of the field is chosen as $\sigma = 0.3$. Then we use the Gaussian kernel for the reconstruction with the same regularization parameter as above, see Figure 7. This

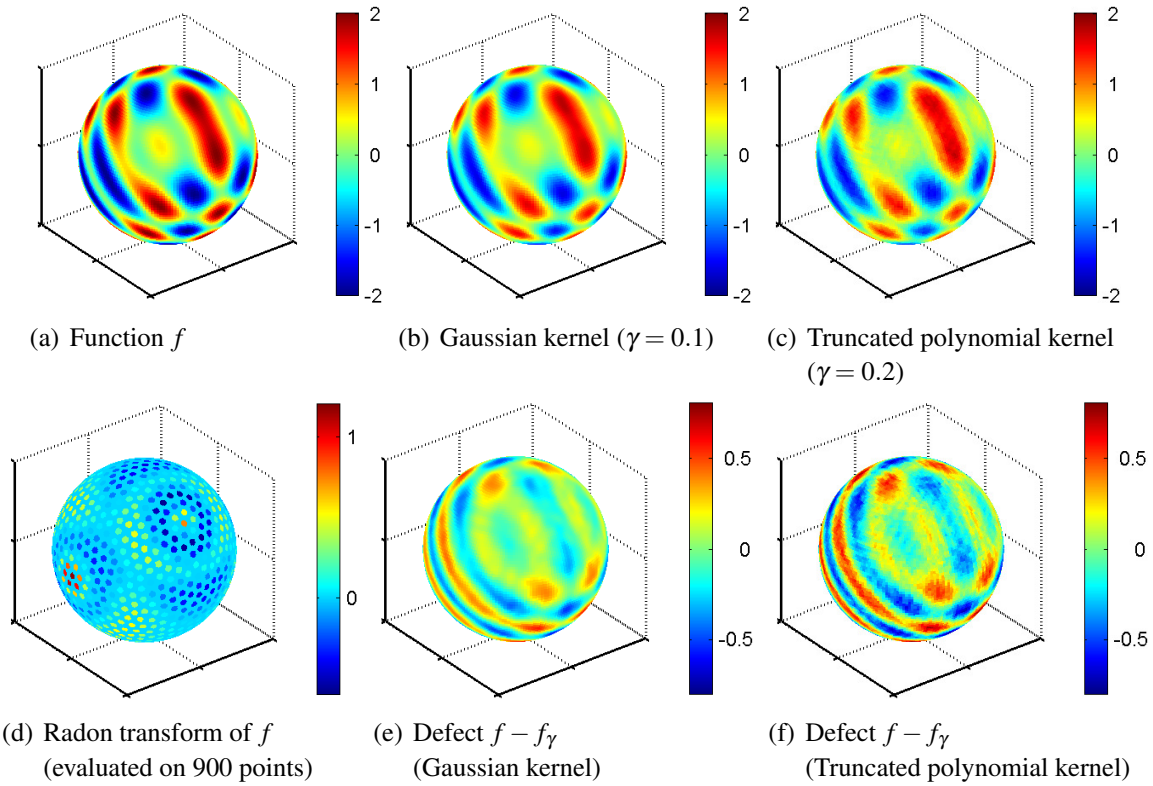

(a) Function f (b) Gaussian kernel ($\gamma = 0.1$) (c) Truncated polynomial kernel ($\gamma = 0.2$)

(d) Radon transform of f (evaluated on 900 points) (e) Defect $f - f_\gamma$ (Gaussian kernel) (f) Defect $f - f_\gamma$ (Truncated polynomial kernel)

Figure 6. Reconstructions from exact data

clearly illustrates that our algorithm works well with disturbed data (because of the build-in regularization).

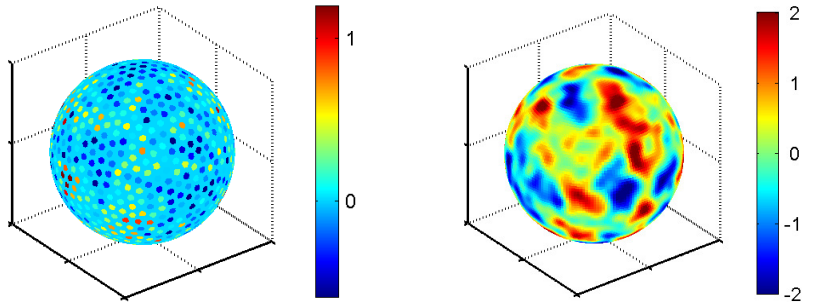

(a) Radon transform of f with normal noise ($\sigma = 0.3$) (b) Reconstruction of f from noisy data ($\gamma = 0.1$)

Figure 7. Reconstruction from noisy data with Gaussian kernel

For the last test we assume that we can observe the Radon transform on only 225 data points. In this case we also get a good reconstruction (Figure 8). If the reconstruction kernel is pre-calculated, which is possible independently of the right hand side g, all reconstructions can be performed in less than two seconds of computing time on a PC (CPU: E8400, RAM: 4 GB). So the computational costs are very low and also higher resolutions can be handled within a reasonable time.

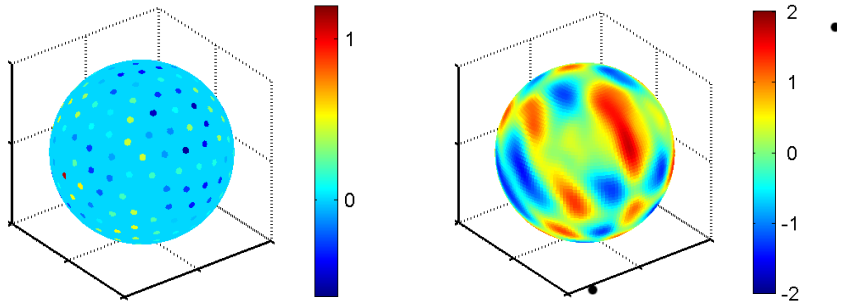

(a) Radon transform (evaluated on 225 points)

(b) Reconstruction ($\gamma = 0.12$) (and stabilized integration)

Figure 8. Reconstruction from few data

7.4. Inversion of the cosine transform in 3D

7.4.1. Reconstruction of a phantom function In this subsection we illustrate the results of our algorithms for the inversion of the cosine transform in case of synthetic data. Figure 9 shows a test phantom and its cosine transform. Due to the higher ill-posedness of the cosine transform compared to the Radon transform, the inversion is more difficult. To have a better view of the results, we have changed the colour map a little in Figure 10. In case of exact data, the three circles on the equator can be reconstructed and also the circular ring near the poles. But for noisy data, the error being about one percent, the left of the three circles is not visible in the reconstruction anymore. Here, we used only 900 data points for the reconstruction. If we increase the number of data points to 3600, all circles can be spotted in the reconstruction (see Figure 10).

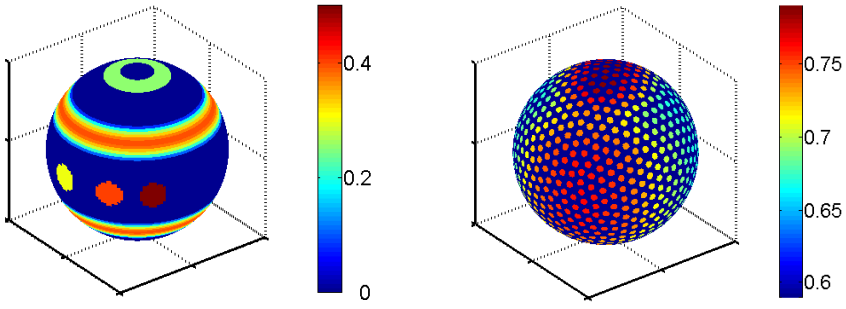

(a) Phantom

(b) Cosine transform of the phantom

Figure 9. Phantom function on the unit sphere used for the inversion of the cosine transform

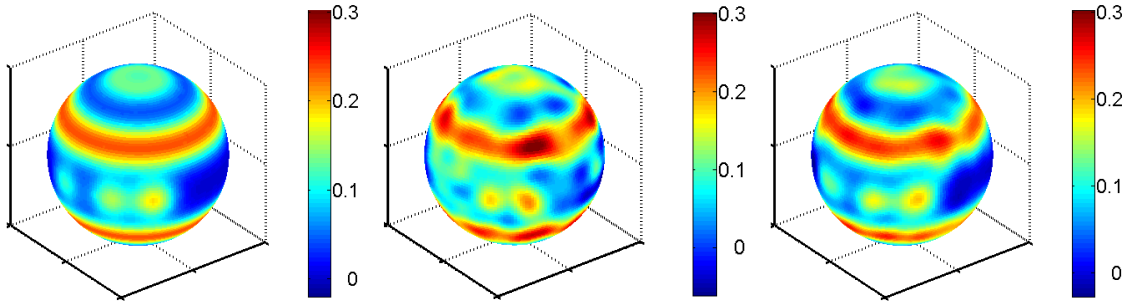

(a) Reconstruction from exact data (b) Reconstruction from noisy data (900 directions) ($\sigma = 0.01$) (c) Reconstruction from noisy data (3600 directions) ($\sigma = 0.01$)

Figure 10. Reconstructions of the phantom from its cosine transform.

7.4.2. Reconstruction of directional distributions In this subsection, we use our algorithm for the inversion of the cosine transform to estimate the directional distribution of stationary cylinder processes from intersections of their cylinders with planes. We have carried out simulation studies in two different settings to show the effectiveness of our method.

In the first experiment we have simulated cylinder processes in the observation window $b(0,1)$. We assume that all information about each cylinder of the process is available for the counting of the intersections. Thus, for each measuring direction η we have intersected the process with the orthogonal plane $\eta^{\perp}$ and analytically determined the number of intersections. Finally, we use the method described in Section 5 and (1) to estimate the directional distribution of the cylinder process. For all reconstructions, we use the regularization parameter $\gamma = 0.22$.

First we consider cylinder processes with a mixed von Mises-Fisher directional distribution. A von Mises-Fisher distributed random vector has the density $f_{\mu,\kappa}(x) = c(\kappa)\exp(\kappa\langle\mu,x\rangle)$, where $c(\kappa) = \frac{\sqrt{\kappa}}{(2\pi)^{3/2}I_{1/2}(\kappa)}$ and I_r denotes the modified Bessel function of first kind and order r. We consider the following symmetric mixed distribution with three peaks: $f(\eta) = \frac{1}{6}\sum_{i=1}^{3}(f_{\mu_i,25}(\eta) + f_{-\mu_i,25}(\eta))$, where $\mu_1 = 1/\sqrt{1.02}(1,0.1,-0.1)^T$, $\mu_2 = (0,1,0)^T$ and $\mu_3 = \sqrt{4/17}(-1,-1.5,1)^T$.

Figure 11 shows the estimates. In some experiments, mainly if the intensity of the process is low, small negative values may appear in the reconstructions. But they only appear in small regions, where the value of the density of the directional distribution is nearly zero, so it should be no problem to neglect these values. Another possibility to overcome this problem is to increase the regularization parameter until all values are positive. The price for this is a loss in resolution. In the majority of cases the estimated integral of the reconstruction over the sphere lies between 0.975 and 1.025 in the case of process intensity 1000. It should be mentioned that these data sets are generated by only one simulation of the cylinder process, so they can be seen as strongly perturbed data.

As a second example we consider the directional fibre distribution introduced in [35], which is used in modelling foams or granular porous media. The density of the directional

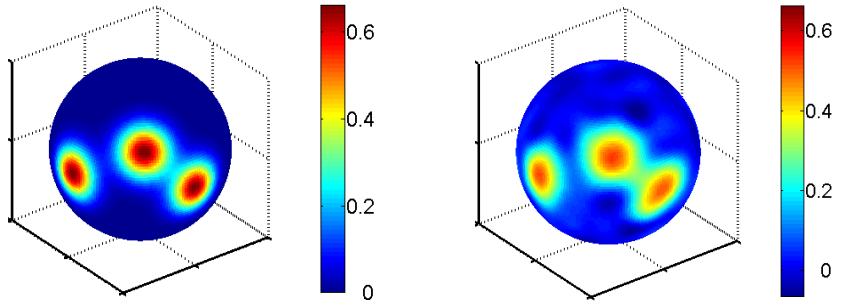

(a) Density function (b) Reconstruction (intensity = 1000)

Figure 11. Mixed von Mises-Fisher distribution

distribution, which is independent of the azimuth angle ϕ, is given by

$$p(\phi,\theta) = \frac{\beta}{4\pi\left[1+(\beta^2-1)\cos^2\theta\right]^{3/2}}, \quad \theta \in [0,\pi]. \tag{24}$$

The parameter β is called *anisotropy parameter*. In the case $\beta = 1$ this is the density of the directional distribution of an isotropic cylinder process. For increasing β, the fibres tend to be more and more parallel to the xy-plane (the material plane). We choose $\beta = 3$ in our experiment. Figure 12 shows the density function and its reconstruction based on one or 5 realizations respectively of the corresponding cylinder process.

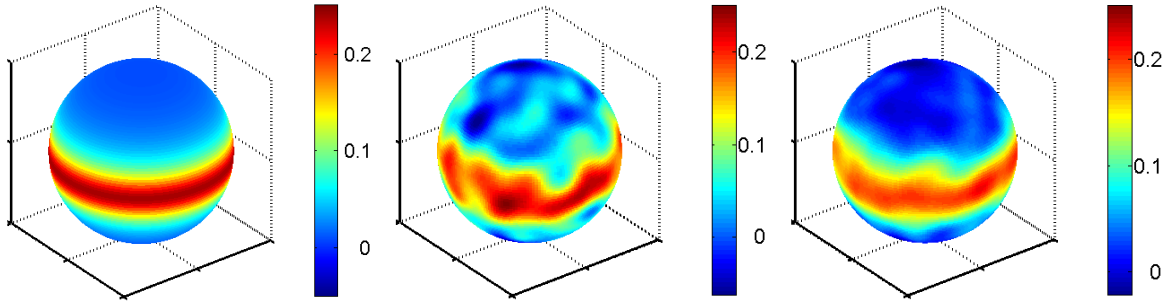

(a) Density function (b) Reconstruction from one realization (c) Reconstruction from 5 realizations

Figure 12. Reconstruction of the distribution defined in (24)

In a further experiment, we have simulated cylinder processes with radius 0.005 and different directional distributions and intensity 500 in the unit cube. The union sets of these cylinder processes have been voxelized with a resolution of 500 voxels per unit length to generate a setting similar to the analysis of microscopic images.

Counting the intersection points of a plane with the voxelized image is a rather difficult task, since cylinders which are (almost) parallel to the plane may be counted multiple times, while overlapping cylinders may be counted only once. Unfortunately, this effect also depends on the direction of the plane, so with the approach to discretize the plane and count the intersections in the resulting images it seems impossible to generate estimates without heavy systematical bias.

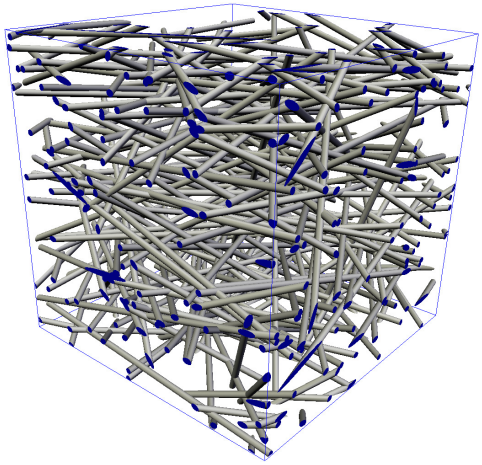

Figure 13. Cylinder process in the unit cube with directional distribution as defined in (24) ($\beta = 3$), intensity 200 and cylinder radius 0.01

To overcome this problem, we have skeletonized the data with the 3D image analysis software Avizo and estimated the intersection intensities with the resulting skeleton. Here we have also computed the values for 900 directions.

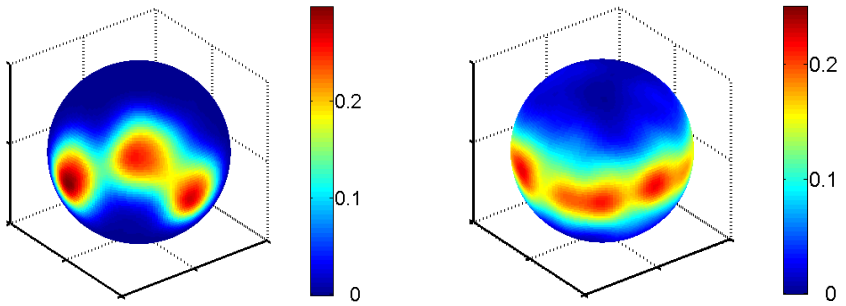

(a) Mixed von Mises distribution (b) Distribution as defined in (24)

Figure 14. Reconstruction from voxelized data

8. Application to real data

In the following, we present the results of our algorithm applied to real microscopic data. For this purpose, we examine images of the gas diffusion layer of a polymer electrolyte membrane fuel cell (with kind permission of the Centre for Solar Energy and Hydrogen Research, Ulm).

For both the two- and the three-dimensional data we have first applied the skeletonization algorithm of Avizo, then estimated the rose of intersections analytically with the resulting set of line segments, and finally applied our method to approximately invert the cosine transform.

8.1. Two-dimensional microscopic images

In this section, we analyze 10 electron microscopic images of 10 different gas diffusion layers of the same kind. One of them can be seen in Figure 1(a). Each has a resolution of 1024 x 696 pixels and shows different layers of the fibre tissue. The fibres are approximately 6 pixels thick.

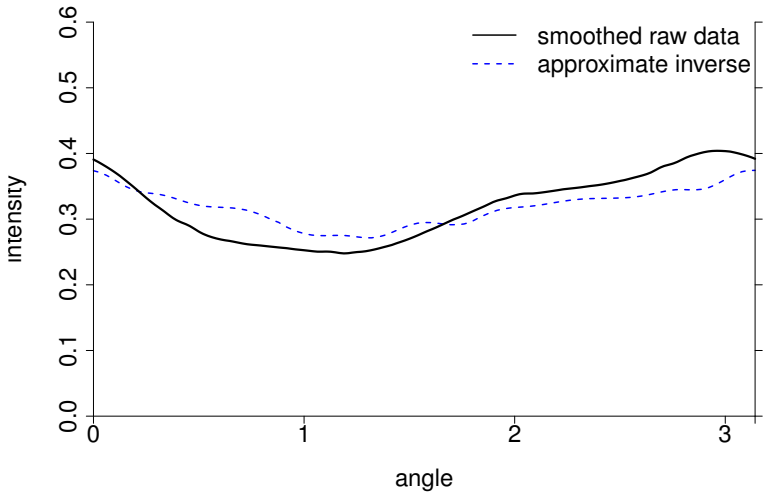

Figure 15. Smoothed data from the line segments of the skeleton and the result of our algorithm

In Figure 15 we present the result of our reconstruction compared to a kernel density estimation based on the directions of the lines and weighted with the length of the lines of the skeleton. This shows that our method works well to reconstruct the directional distribution of two-dimensional real data, as the result of our method is very close to the original data from the skeletonization.

8.2. Three-dimensional synchrotron images

Here, we reconstruct the directional distribution of one synchrotron image with a resolution of approximately 1000 x 1000 x 200 voxels, see also Figure 1(b), where a cut-out of the skeleton generated by Avizo can be seen.

Because of the production process the directional distribution of the fibres should be approximately isotropic w.r.t. the x-y plane, which is also shown in our reconstruction. As it can be seen in the smoothed raw data (i.e. the directions and lengths of the segments) from the Avizo skeleton in Figure 16(a), again there is an artifact in the reconstruction from the skeletonization, the values at the axis directions are too low, whereas at the bisector they are too high. Of course, this can be seen in our reconstruction (cf. Figure 16(b)) as well, although this is not a problem of our method but of the input data. Thus, this shows that our method works well on real three-dimensional data.

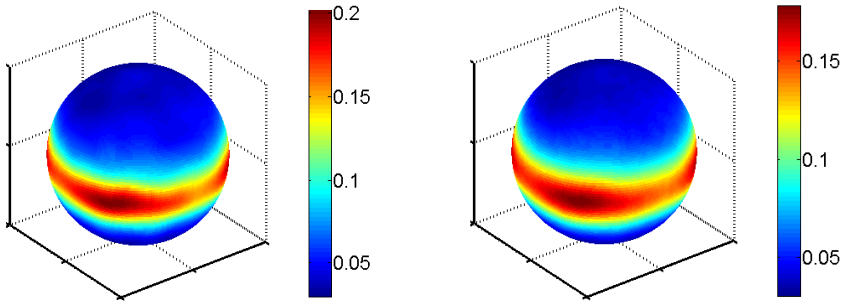

(a) Kernel density estimation, based on the raw data

(b) Reconstruction with the approximate inverse method

Figure 16. Reconstruction from real data ($\gamma = 0.22$), both reconstructions are based on the skeleton generated by Avizo

Acknowledgments

Our research has been supported by a grant of the German Research Foundation (DFG). We want to thank Markus Kiderlen for fruitful discussions.

[1] M. Kiderlen and A. Pfrang. Algorithms to estimate the rose of directions of a spatial fiber system. *J. Microscopy*, 219(2):50–60, 2005.

[2] L.M. Hoffmann. Estimating an even spherical measure from its sine transform. *Appl. Math.*, 54(1):67–78, 2009.

[3] R. Gardner, M. Kiderlen, and P. Milanfar. Convergence of Algorithms for Reconstructing Convex Bodies and Directional Measures. *Ann. Statist.*, 34(3):1331–1374, 2006.

[4] R. J. Gardner. *Geometric Tomography*, volume 58 of *Enc. of Mathematics and its Appl.* Cambridge University Press, 1995.

[5] H. Groemer. *Geometric Applications of Fourier Series and Spherical Harmonics*. Cambridge University Press, New York, 1996.

[6] P. Goodey and W. Weil. Centrally symmetric convex bodies and the spherical Radon transform. *J. Differential Geom.*, 35:675–688, 1992.

[7] R.S. Strichartz. L^p estimates for the Radon transforms in Euclidean and non-Euclidean spaces. *Duke Math. J.*, 48:699–727, 1981.

[8] S. Helgason. *Geometric Analysis on Symmetric Spaces*. AMS, 2nd edition, 2008.

[9] E. Spodarev. On the rose of intersections for stationary flat processes. *Adv. Appl. Probab.*, 33(3):584–599, 2001.

[10] B. Rubin. Inversion formulas for the spherical Radon transform and the generalized cosine transform. *Adv. in Appl. Math.*, 29:471–497, 2002.

[11] A.K. Louis and P. Maaß. A mollifier method for linear operator equations of the first kind. *Inverse Problems*, 6:427–440, 1990.

[12] T. Schuster and E.T. Quinto. On a regularization scheme for linear operators in distribution spaces with an application to the spherical Radon transform. *SIAM J. Appl. Math.*, 65(4):1369–1387, 2005.

[13] A.K. Louis. Combining image reconstruction and image analysis with an application to two-dimensional tomography. *SIAM J. Imaging Sci.*, 1(2):188–208, 2008.

[14] A. Lakhal and A.K. Louis. Locating radiating sources for Maxwell's equations using the approximate inverse. *Inverse Problems*, 24 (045020)(4), 2008.

[15] M.K. Likht. Calculation of functionals on the solutions of linear equations of the first kind. *USSR Comput. Math. and Math. Phys.*, 7(3):271–278, 1967.

[16] J. E. Hilliard. Specification and measurement of microstructural anisotropy. *Trans. of the Metallurgical Soc. of Aime*, 224:1201–1211, 1962.

[17] J. Mecke. Formulas for stationary planar fibre processes III – Intersections with fibre systems. *Math. Operationsforsch. Statist. Ser. Statistik*, 12:201–210, 1981.

[18] D. Stoyan, W. S. Kendall, and J. Mecke. *Stochastic Geometry and its Applications*. J. Wiley & Sons, Chichester, 2nd edition, 1995.

[19] T. Schuster. *The method of approximate inverse: theory and applications*, volume 1906 of *Lecture Notes in Mathematics*. Springer, 2007.

[20] R. Gorenflo and S. Vessella. *Abel integral equations (analysis and applications)*. Springer, 1991.

[21] Gradshteyn I.S. and Ryzhik I.M. *Table of integrals, series, and products*. Academic press San Diego, 1996.

[22] P. Jonas and A.K. Louis. A Sobolev space analysis of linear regularization methods for ill-posed problems. *J. Inverse Ill-Posed Probl.*, 9(1):59–74, 2001.

[23] R. Kress. *Linear integral equations*. Springer, 1999.

[24] H. Wendland. *Scattered data approximation*. Cambridge University Press, 2005.

[25] W. Freeden and M. Schreiner. *Spherical Functions of Mathematical Geosciences: A Scalar, Vectorial, and Tensorial Setup*. Springer, 2008.

[26] V.A. Menegatto. Approximation by spherical convolution. *Numer. Funct. Anal. Optim.*, 18(9):995–1012, 1997.

[27] M. Spiess and E. Spodarev. Anisotropic dilated Poisson k-flat processes. *Methodol. Comput. Appl. Probab.*, 2010. (to appear).

[28] W. Weil. Point processes of cylinders, particles and flats. *Acta Appl. Math.*, 9:103–136, 1987.

[29] J. Mecke and W. Nagel. Stationäre räumliche Faserprozesse und ihre Schnittzahlrosen. *Elektron. Informationsverarb. Kybernet.*, 16:475–483, 1980.

[30] H. Digabel. Détermination pratique de la rose des directions. In *15 Fasicules de morphologie mathématique appliqué*, chapter 6. Fontainebleau, 1975.

[31] J. Rataj and I. Saxl. Estimation of direction distribution of a planar fibre system. *Acta Stereologica*, 11:631–636, 1992. Suppl. I.

[32] R.H. Hardin and N.J.A. Sloane. McLaren's improved snub cube and other new spherical designs in three dimensions. *Discrete Comput. Geom.*, 15(4):429–441, 1996.

[33] J. Fliege and U. Maier. The distribution of points on the sphere and corresponding cubature formulae. *IMA J. Numer. Anal.*, 19(2):317–334, 1999.

[34] I.H. Sloan and R.S. Womersley. Extremal systems of points and numerical integration on the sphere. *Adv. Comput. Math.*, 21(1):107–125, 2004.

[35] K. Schladitz, S. Peters, D. Reinel-Bitzer, A. Wiegmann, and J. Ohser. Design of acoustic trim based on geometric modelling and flow simulation for non-woven. *Computational Materials Science*, 38(1):56–66, 2006.